A Semi-Numerical Finite Element Post-Processing Torque Ripple Analysis Technique for Synchronous Electric Machines Utilizing The Airgap Maxwell Stress Tensor

C.M.Spargo[1], *Member, IEEE and* B. C. Mecrow[1], *Member, IEEE* and J. D. Widmer[1]

[1]School of Electrical and Electronic Engineering, Merz Court, University of Newcastle Upon Tyne, UK

A novel method to calculate the harmonic torque components in synchronous machines is presented. Harmonic torque components create a torque ripple, which is undesirable in many applications. This torque ripple is a major cause of acoustic noise and vibration and can limit the machine's application range. A semi-numerical method is developed to calculate and analyse harmonic torque components based on Maxwell stress tensor theory. Development of the Maxwell stress expressions leads to a simple algebraic expression for the calculation. Finite element (FE) analysis is used to determine the equation variables. It is shown that post-processing of the FE solution provides valuable information regarding the composition of the torque waveform, based upon field harmonics and, which was previously unavailable. A deeper insight can be gained into more direct electromagnetic design changes to reduce torque ripple in synchronous machines, improving their torque quality. As an example, the developed method is applied to a synchronous reluctance machine with fractional slot, concentrated windings that is known to exhibit high torque ripple.

***Index Terms*— Fractional slot concentrated windings, finite element method, Maxwell stress tensor, harmonics, synchronous reluctance machine, torque pulsation.**

I. INTRODUCTION

TORQUE ripple is a major concern in electrical machines, causing unwanted acoustic noise and vibration [1] as well as limiting the application range of the machine to applications where torque quality is of low importance. Effective reduction in torque ripple is an important consideration and challenge for electrical machine designers. Torque ripple analysis, and therefore mitigation, is limited with finite element solutions as no information relating to the composition or cause can be explicitly found, only the resultant torque waveform. The mean torque and torque ripple are the only figures of merit that can be determined by conventional methods, with percentage torque ripple assessing the torque quality. Detailed information would be useful to machine designers in order to assist iterative geometry selection associated with practical machine design. Although there are many papers focusing on torque ripple reduction in synchronous machines, the majority of which suggest design changes [2-6], others concentrate on the drive and control aspect of reducing torque ripple [7-9]. The sources affecting torque ripple can be defined:

1. Cogging
2. Stator MMF and permeance interaction
3. Stator MMF and back EMF interaction

The cogging torque is due to special variations in permeance caused by stator slotting and is only applicable in machines with permanent magnets, therefore is not present in synchronous reluctance machines. The second source is applicable in all salient synchronous machines and is most evident in machines with a high level of MMF space harmonic content. The third source is applicable again only to permanent magnet machines where a non-sinusoidal back EMF exists or the excitation current is non-sinusoidal. These sources affect the harmonic content of the waveform, which leads to the torque ripple, acoustic noise and vibration. Fractional slot concentrated windings (FSCW) are now common in permanent magnet synchronous machines [10-13], and have been preliminarily investigated in induction machines and also synchronous reluctance machines by the authors [14], where they are known to have high levels of torque ripple. FSCWs offer a multitude of advantages to the machine designer, including [11]:

- Non-overlapping end windings
- Short end windings
- Higher slot fill factor
- Stator modularity and ease of manufacture

These advantages lead to lower copper loss and mass, higher slot thermal conductivity, active length reduction and higher performance [14]. In a detailed review [10] a compelling argument for the transition from distributed windings to FSCW is presented. However, the advantages of FSCW can be overshadowed by the rich harmonic content in the resultant MMF waves. These lead to unwanted parasitic effects, such as torque ripple, through stator MMF and permeance variation interaction. The harmonic content derives from the winding factors of particular winding patterns, which in turn depend on the number of poles and the stator tooth number [15]. Harmonic analysis of FSCW MMF waves and analysis of their effects on PMSM performance is detailed in [16]. These analyses are based on analytical methods, which do not have the same accuracy as the finite element method. No harmonic analysis of FSCW synchronous reluctance (cSynRM) machines is, to the authors' best knowledge, found in the literature. In [14] the authors' presented the first analysis of a cSynRM machine in comparison with a conventional polyphase distributed winding synchronous reluctance machine. They concluded that in order to improve the performance of this type of machine, the torque ripple must be analysed and reduced before it can compete with machine types with a low torque ripple.

The aim of the paper is to develop a semi-numerical post-processing tool to calculate the harmonic torque components. This tool is then applied to a fractional slot concentrated winding synchronous reluctance machine that is known to have a large torque ripple, in order to determine electromagnetic design changes so that the torque quality can be improved. Although this example application is provided, it is beyond the scope of this paper to detail the complete electromagnetic design processes and is provided to illustrate the possibilities of the developed post-processing method.

II. Applicable Winding Harmonics

Synchronous reluctance machines are universally designed with either an integer or fractional slot polyphase winding [17-19]. The fractional slot concentrated (FSCW), is defined by the number of slots per pole per phase, q;

$$q = \frac{Q_s}{2mp} = \frac{z}{n} \tag{1}$$

Where Q_s, is the number of stator slots, p is the number of pole pairs and m is the number of phases. The terms z and n represent the numerical value of the fraction's numerator and denominator. If $q < 1$ the winding is a fractional slot concentrated winding. The FSCW can be split into two grades, depending upon n in a fractional q [15]; Grade I if n is even, which implies asymmetrical flux over a pole and Grade 2 if n is odd where symmetry exists over the pole. The grade of the winding affects the winding factors of the winding and thus directly affects the MMF harmonics and therefore the airgap field harmonics. The applicable harmonics are defined by;

$$v = \begin{cases} n^{-1}(2mg+2) - G\text{rade I} \\ n^{-1}(2mg+1) - G\text{rade II} \end{cases} \text{ for } g = 1,2,3,4 \ldots \tag{2}$$

Odd and even harmonics can exist within FSCW machines. Usually the even harmonics are eliminated by the symmetry of a sinusoidally distributed integer or fractional slot winding. However, FSCWs can set up asymmetrical field waveforms due to the distribution of the coils and it must be noted that if q is < 1, the resulting flux waveform in the machine may be asymmetrical and if q is ≤ 0.5, the main flux path in the machine in the air gap region may consist of one slot and one tooth leading to significant asymmetry and space harmonic content. Also, if $z \neq 1$, sub-harmonics will exist in the winding factors and will contribute to the MMF. The winding factors ξ_v are used in the calculation of the machine harmonic MMF content, are calculated as [20];

$$\xi_v = \begin{cases} \sin\left(\frac{\pi p}{Q_s}\right) \frac{\sin\left(\frac{v\pi}{2m}\right)}{nq \sin\left(\frac{v\pi}{2mnq}\right)} - \text{Grade I} \\ \sin\left(\frac{\pi p}{Q_s}\right) \sin\left(\frac{v\pi}{2m}\right) \frac{\cos\left(\frac{v\pi}{Q_s}\right)}{nq \sin\left(\frac{v\pi}{2mnq}\right)} - \text{Grade II} \end{cases} \tag{3}$$

Usually a winding is selected that eliminates or reduces higher order harmonics, but retains a high fundamental winding factor. We can do the same in FSCWs, however in some cases it is noted that no higher order harmonic reduction or elimination is possible. This leads to high winding factors for harmonics, with the same magnitude as the fundamental. The harmonic content of a concentrated winding is higher than that of a distributed winding, as presented in Fig. 1. This leads to design challenges for optimum performance, which includes high levels of torque ripple components.

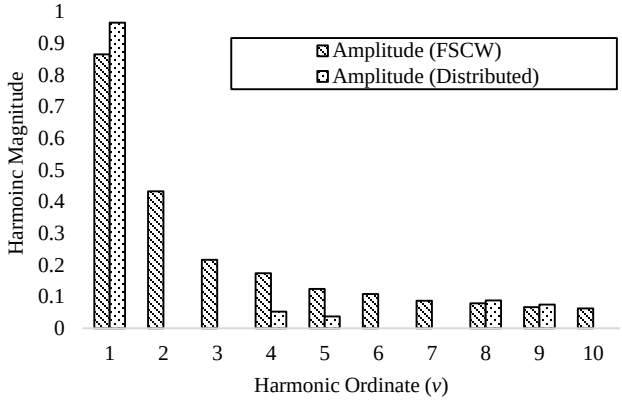

Fig. 1. MMF harmonics of a 36 slot, 4 pole integer slot distributed winding and MMF harmonics of a 6 slot, 4 pole fractional slot concentrated winding.

III. MMF Harmonics

The stator MMF in an electrical machine is important in torque production; it is especially important in reluctance machines as it also serves as a magnetizing force. The resultant MMF in the air gap is a function of space and time which can be written as rotating waves [16];

$$F_m(\theta,t) = \sum_{v=1}^{\infty} \sum_{c=1}^{n_c} \frac{4N\xi_v}{vp\pi} \{F_{mv}^{+}(\theta,t) + F_{mv}^{-}(\theta,t)\} \tag{4}$$

Where N the number of series turns per phase and ξ_v is the harmonic winding factor. The forwards F_{mv}^{+} and backwards F_{mv}^{-} rotating harmonic MMF components can be written as co-sinusoidal waves in space and time. The stator MMF waves interact with the machine permeance function (a function of space and time also) to form the air gap flux and also produce the torque ripple components. Therefore it is key, in order to reduce machine losses, torque ripple, acoustic noise, and vibration, to minimize the harmonic content in the air gap flux.

IV. Field Harmonics

Calculation of both winding factors and MMF is readily performed analytically from eq. (3) and eq. (4) with applicable harmonics given by eq. (2). Accurate calculation of airgap magnetic fields is difficult to determine analytically, due to permeance variation, saturation and other effects. Performing transient with motion FE analysis at the desired operating points, we can then extract the air gap field, defined by an arc in the center of the air gap. As the air gap is small, the

assumption is made that the variation across the air gap in the radial dimension is negligible. The airgap flux density can be discretized and extracted;

$$\mathbf{B} = B_\theta + jB_r \tag{5}$$

Where B_θ and B_r are the tangential and radial magnetic flux density components around the airgap circumference as a discrete function of time and space;

$$\mathbf{B} = \mathbf{B}\,[\theta, t] \tag{6}$$

The angle around the airgap is discretized according to;

$$\theta = n\left(\frac{2p}{N}\right);\ \text{where n} = 1,2,3,\dots N-1 \tag{7}$$

Where n is the discrete sample index and N is the number of samples. The radial and tangential components, around the air gap at each point in time can then be decomposed using a discrete time Fourier series;

$$B[v] = \frac{1}{N}\sum_{n=0}^{N-1} |B[\theta]|\, e^{-ivn\left(\frac{2\pi}{N}\right)} \tag{8}$$

It can be shown that the inverse transform of eq. (8) can be represented;

$$B[\theta] = 2\sum_{v=1}^{\left(\frac{N}{2}\right)-1} |B[v]| \cos(v\Omega_0\theta) \tag{9}$$

Evaluation of the field around the air gap at each time instant is performed to obtain the time varying magnetic field used for torque waveform calculation and calculation of the harmonic torque components. The term $\Omega_0 = \frac{2\pi}{N}$, is the discrete angle.

V. Maxwell Stress Torque Calculation

The Maxwell stress tensor [22] is extensively used in the calculation of torque in electromagnetic machines [23]. The tensor expressed in cylindrical coordinates and neglecting any *z*-axis component field due to 2D finite element studies, the resultant shear rotor stress is written;

$$\sigma(\theta, t) = \frac{B_\theta(\theta, t)B_r(\theta, t)}{\mu_0} \tag{10}$$

This tangential stress allows calculation of the resultant rotor electromagnetic torque at a time instant by integrating over the surface;

$$T_\theta(t) = \frac{r^2}{\mu_0}\int_0^{l_a}\int_0^{2\pi} B_\theta(\theta, t)B_r(\theta, t)\, d\theta dz \tag{11}$$

It must be noted that this expression allows calculation of only the *total* or *resultant* electromagnetic torque developed by the machine, based on this conventional calculation, and contains no information on harmonic torque components due to airgap field harmonics.

VI. Torque Contribution by Field Harmonics

The radial and tangential fields are functions of the air gap periphery angle and can be harmonically decomposed and reassembled as a sum of cosinusoidal functions according to eq. (9). In the continuous domain, this sum can be written for either the radial or tangential fields for an instant in time as;

$$B(\theta) = 2\sum_{v=1}^{\infty} |B_v| \cos(v\theta + \widehat{\varphi_v}) \tag{12}$$

Where $\widehat{\varphi_v}$ is the harmonic phase of the harmonic v, therefore each harmonic field is expressed;

$$B_v(\theta) = 2|B_v| \cos(v\theta + \widehat{\varphi_v}) \tag{13}$$

An expression for the harmonic air gap tangential stress (force density) can then be formed for use in harmonic torque calculations.

$$\sigma_\theta^n(\theta) = \frac{4}{\mu_0}|B_l| \cos(l\theta + \widehat{\varphi_l})|B_m| \cos(m\theta + \widehat{\varphi_m}) \tag{14}$$

Where l and m are used as the harmonic ordinates for the tangential and radial fields and n is the resultant harmonic of the tangential stress. The resultant shear stress can be found by a simple summation due to the superposition theorem.

$$\sigma_\theta(\theta) = \sum_{n=1}^{\infty} \sigma_\theta^n\,(\theta) \tag{15}$$

Then development of an equation providing information on harmonic torque components by substitution of eq. (14) into eq. (11) follows. Using trigonometric identities and setting for convenience $\widehat{\varphi_l} = 0$ in the equation and then define $\varphi_d \triangleq \widehat{\varphi_l} - \widehat{\varphi_m}$, integrating over the machine length l_a noting that the integral only exists when *l=m=v;*

$$T_\theta^n = \left(\frac{4l_a r^2}{\mu_0}\right)\frac{\sin(2v\theta + \varphi_d^v) + 2v\theta\cos(\varphi_d^v)}{4v}\Bigg|_{\theta=0}^{\theta=2\pi}$$

$$= \left(\frac{4l_a r^2}{\mu_0}\right)\left(\frac{\sin(4\pi v + \varphi_d^v) - \sin(\varphi_d^v)}{4v} + \pi\cos(\varphi_d^v)\right) \tag{16}$$

Then by analysis, for $v = 1,2,3,4 \dots \Rightarrow \sin(4\pi v + \varphi_d^v) \rightarrow \sin(\varphi_d^v)$, thus the first term in eq. (16) disappears and the harmonic torque equation is now a simple equation;

$$T_\theta^n = \frac{4\pi l_a r^2}{\mu_0}|B_r^v|\,|B_\theta^v| \cos(\varphi_d^v) \tag{17}$$

Where $|B_r^v|$ is the magnitude of the radial field *v*th harmonic, $|B_\theta^v|$ is the *v*th harmonic of the tangential field, which are either forwards or backwards rotating harmonic fields, and φ_d^v is the phase angle between the *v*th harmonic of the radial and tangential fields. The factor '4' in the equation comes from eq. (9) regarding the DTFS decomposition of the field components from the finite element solution, it is not physically significant. Eq. (17) allows harmonic torque calculation for each point in time or rotor angle. From this, the resultant torque can be calculated at a time instant and if a time stepping transient with motion study is performed, the individual airgap field harmonics contribution to torque production can be charted, providing valuable information. The corresponding resultant torque T_θ at a particular time instant *t*, mean torque $\overline{T_\theta^v}$ over a full mechanical rotation of time interval *t*=0 to *t*=T with N_T time samples and torque ripple are expressed in equations 18 to 20.

$$T_\theta = \frac{4\pi l_a r^2}{\mu_0} \sum_{v=1}^{\infty} |B_r^v|\,|B_\theta^v| \cos(\varphi_d^v) \tag{18}$$

$$\overline{T_\theta^v} = \frac{4\pi l_a r^2}{N_T \mu_0} \sum_{t=0}^{T} \left(\sum_{v=1}^{\infty} |B_r^v|\,|B_\theta^v| \cos(\varphi_d^v) \right)_t \tag{19}$$

$$T_\theta^{\%} = \frac{\max_{\forall t}(T_\theta) - \min_{\forall t}(T_\theta)}{\overline{T_\theta^v}} \times 100\% \tag{20}$$

This set of equations, along with eq. (17) provide the framework for a finite element post processing technique to provide detailed information of the torque quality of synchronous machines. It is observed that $\pi l_a r^2$ is equal to the rotor electromagnetic volume.

VII. FSCW Synchronous Reluctance Machine

Fractional slot concentrated windings can be applied to synchronous reluctance machines [14]. Due to the dependence of the machine magnetizing current upon the pole number, a low pole number is generally used. This limits the slot-pole combinations available: in this paper a 6 slot, 4 pole machine is analysed (Fig.2) and electromagnetic design changes made in order to reduce the known torque ripple in this slot-pole combination, which has been chosen as to illustrate the method. The machine utilizes single tooth windings to achieve low copper loss, high efficiency and torque density. The number of slots per-phase-per-pole is;

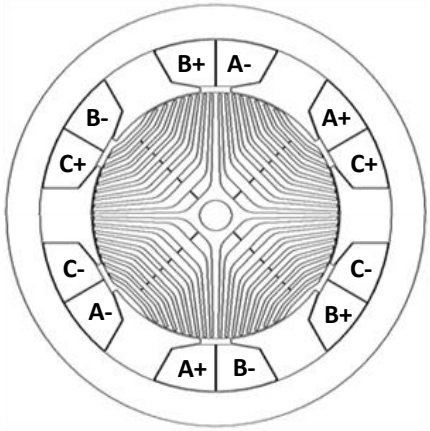

Fig. 2. The 6-slot 4-pole synchronous reluctance machine under consideration in this study.

$$q = \frac{6}{(2)(3)(2)} = \frac{z}{n} = \frac{1}{2} \tag{21}$$

The denominator *n* is 2, which is *even* and thus the winding is categorized as a Grade I winding with harmonics given by;

$$v = (3g + 1) \text{ where } g = 1,2,3,4 \ldots \tag{22}$$

So *v* takes on the values, 1, -2, 4, -5, 7 … etc. The significance of the *–ve* is that these harmonics are counter-rotating harmonics with respect to the fundamental. The winding factors are calculated and the MMF per-unit magnitudes are also calculated from eq. (3) and eq. (4) are depicted in Fig. 3. It can be seen that the machine has constant winding factors, due to $\sin\left(\frac{v\pi}{2m}\right) \backslash nq \sin\left(\frac{v\pi}{2mnq}\right) = 1$ in eq. (3) because $q = \frac{1}{2}$ and $n = 2$. Therefore, there are high magnitude harmonic MMF components available for interaction with the rotor permeance, causing the unwanted parasitic effects. These harmonic effects can also be determined graphically by Fourier analysis of the MMF function, presented in Fig. 4, where the MMF rise over the slot has not been shown. The profile is far from sinusoidal. This MMF space harmonic content is represented in the airgap magnetic field which as according to eq. (17) create harmonic torque components of the order equal to that of the field harmonic. Even harmonics

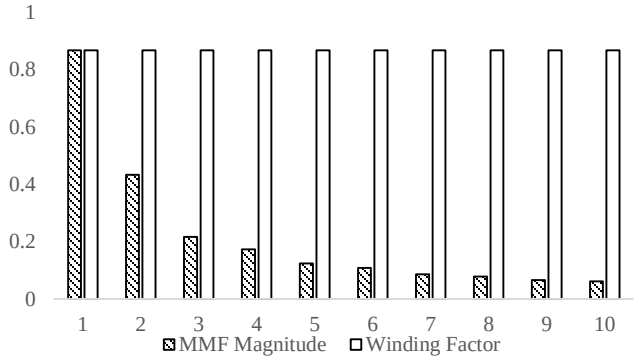

Fig. 3. The winding factors (unshaded) and MMF per-unit magnitudes (shaded) of the 6-slot 4-pole fractional slot concentrated winding synchronous reluctance machine.

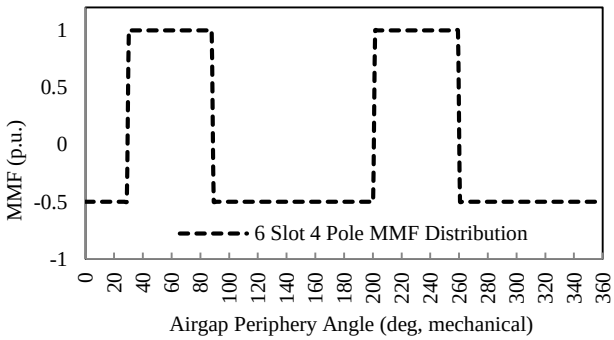

Fig. 4. MMF distribution function of the 6-slot 4-pole fractional slot concentrated winding synchronous reluctance machine (Phase A).

exist in the machine due to the asymmetric flux waveforms resulting from the discrete coil placements. The machine under consideration is operated at its base speed of 1500rpm with a rated current of 20A with a transverse laminated 4-pole flux barrier rotor. The machine has mechanical and winding specifications according to Table. I and Figure 2.

TABLE I
MACHINE CHARACTERISTICS

Parameter	FSCW
Stator outer diameter [mm]	150
Rotor outer diameter [mm]	88
Axial length [mm]	150
Airgap width [mm]	0.5
Pole pairs	2
Stator Slots	6
Slots/Pole/Phase	0.5
Number of phases	3
Series turns	104
Number of coils per phase	2
Turns per coil	52
Number of rotor barriers	5
Fundamental winding factor	0.866
Winding pitch	2/3

The rotor design is not optimized for this stator configuration and from a time stepping finite element solution the torque waveform is calculated at the desired operating point, presented in Fig. 5.

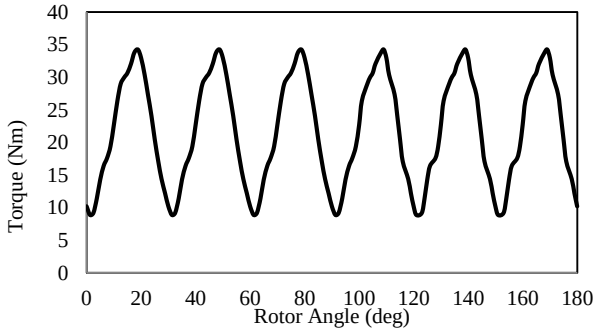

Fig. 5. FE Torque waveforms at rated operating point of the FSCW SynRM.

From the two figures of merit available without the post-processing technique, the torque waveform exhibits a mean torque of 23Nm and a torque ripple of over 100%. This level of torque ripple is unacceptable and is usually found in switched reluctance machines, but not synchronous reluctance machines. As indicated by the authors in another paper [14], analysis and mitigation must be performed in order to realize a practical machine, by improvement in the torque quality.

This machine and winding type has been used in this paper to illuminate the usefulness and accuracy of the method. The method can be further applied to all machine and winding types. The simulated winding is a balanced three phase star-connected winding driven by sinusoidal currents. The sinusoidal currents allow the space harmonic contributions that is of interest here, to be separated from any time harmonic content.

VIII. POST-PROCESSING EXAMPLE

The post-processing technique developed in section VI is now applied. The process is easily automated using interoperability opportunities between software packages through custom scripting. MATLAB® is used as front end application to run the finite element software in the background and to extract the required data-sets and post-process this data based on eqns. (17), (18), (19) and (20).

The developed method is can be incorporated into the motor design cycle. A simplified flow diagram incorporating the technique is presented in Figure 6. The method can be performed iteratively to achieve a reduction in torque ripple, but the technique alone cannot achieve results, the electromagnetic design changes are chosen by the designer given the information obtained from this tool.

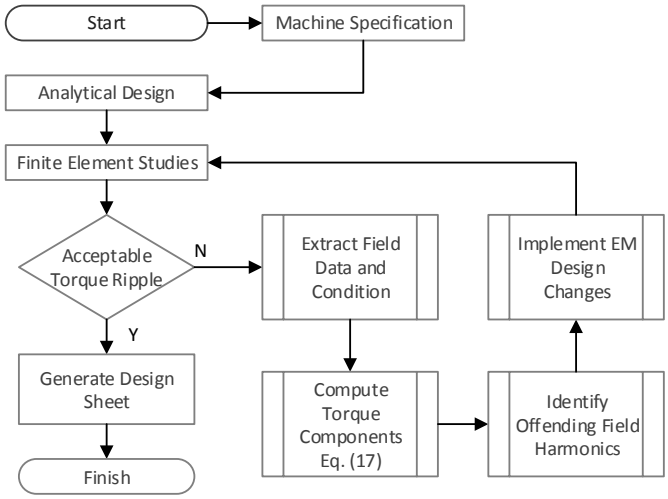

Fig. 6. Simplified relation of the developed post-processing technique to the electromagnetic design process.

The airgap field information extracted in accordance with eq. (7) is tabulated in Table II and visualized in Fig. 7, with the resultant waveforms in Fig. 8. All are at an arbitrary time instant in the electrical cycle.

TABLE II
FIELD HARMONICS AT $t=t_1$

Ordinate	Radial Field Mag (T)	Radial Field Phase (rad)	Tangential Field Mag (T)	Tangential Field Phase (rad)
1	0.737	0.011	0.045	0.445
2	0.359	0.116	0.050	1.955
3	0.038	-0.365	0.005	0.786
4	0.049	1.967	0.024	2.582
5	0.150	-2.738	0.025	-1.580
6	0.066	0.708	0.003	0.204
7	0.059	-2.761	0.009	-1.196
8	0.070	0.228	0.011	1.675
9	0.017	2.603	0.005	2.666
10	0.071	-0.127	0.012	2.148
11	0.015	1.916	0.002	-2.1307
12	0.015	-3.0842	0.003	-0.068

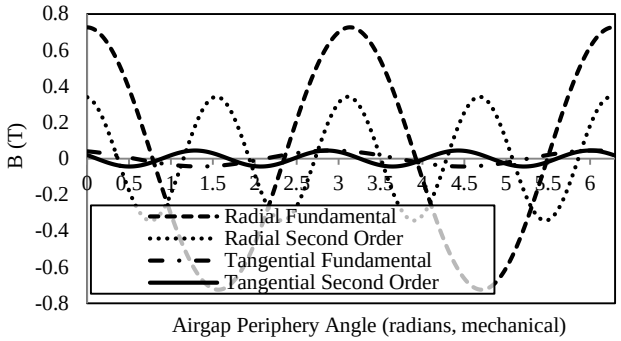

Fig. 7. Harmonic visualization of the fundamental and second harmonics in the radial and tangential fields.

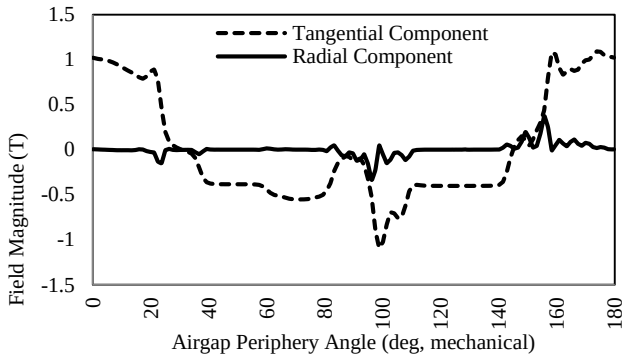

Fig. 8. Radial and tangential airgap field resultant waveforms at $T=T_1$.

It is evident that there is a large second order field component, in other words a counter-rotating 8-pole field with respect to the fundamental 4-pole field. By using the developed equations, calculation of the torque harmonics due to these super-synchronous field components is possible. Particular interest is paid to the second order field component - the majority of the torque ripple is caused by this counter-rotating field, which derives from the space harmonic content in the MMF distribution. This information was previously unobtainable and now drives the direction in reducing the particular harmonic in order to improve the torque quality of the machine. In order to visualize the harmonic torque components over an electrical cycle a diagram of the harmonic field contribution to the torque is presented in Fig. 9.

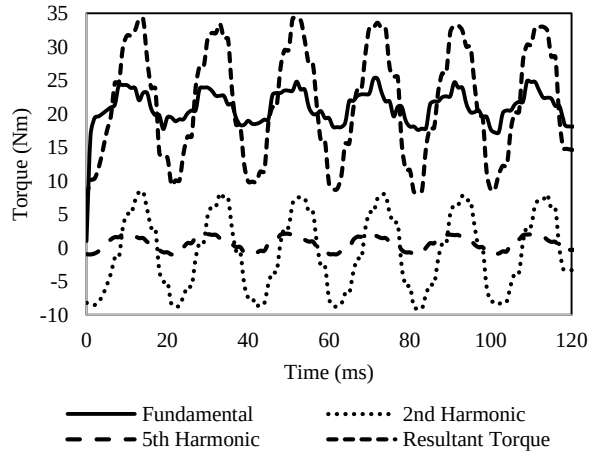

Fig. 9. Significant harmonic torque components over 120ms at 1500rpm, including the resultant torque waveform.

This shows clearly the contribution of the harmonic torque components, by the superposition principle, to the resultant torque waveform. As a final validation of the developed post-processing method, the torque harmonics are reconstructed according to eq. (18), presented in Fig. 10, it shows that the reconstructed waveform based on the superposition of harmonic torque components is a faithful representation of the actual finite element resultant waveform.

The slight differences in the waveform shape and magnitude are caused by the evaluation method of the Maxwell stress tensor in the discretized airgap/sampling issues. Other

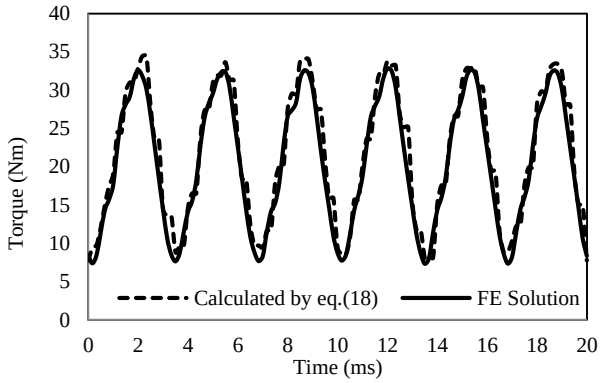

Fig. 10. Comparison of the reconstructed waveform by the developed post-processing method and finite element resultant waveform (20ms = 180 mechanical degrees)

methods of evaluating the stress tensor could give higher accuracy results but it is beyond the scope of this paper to explore these further. This torque ripple must therefore be reduced now we have gained valuable and validated information on its source. In the next section electromagnetic design changes are developed in order to achieve this aim.

IX. Example Rotor Development

The second order (8-pole) field is the root cause of the high level of torque ripple in the machine. This second order field is counter-rotating at a speed relative to the fundamental given by;

$$\omega_{rs} = -\frac{\omega}{2} \tag{23}$$

Where $\omega = 2\pi f_s$. This interacts with the rotor saliency (permeance function), which is designed for 4-pole operation, and torque is produced. The torque is obviously oscillatory as the harmonic field is rotating at ω_{rs}. Therefore, we must reduce the apparent saliency of the rotor for this field, without compromising the saliency for the main torque producing component, the 4-pole field. To do this, consider the FE calculated flux patterns for the 8-pole field in Fig. 11.

By considering the points of maximum and minimum torque production of the travelling 8-pole field and knowing that higher order harmonic fields penetrate less into the iron than lower orders, a slight modification of the rotor in the form of a q-axis cutout, depending upon the harmonic order, could reduce the effective saliency and therefore solve the torque ripple problem. Introducing a q-axis cutout, the resulting mean torque and torque ripple can be evaluated without the developed post-processing technique.

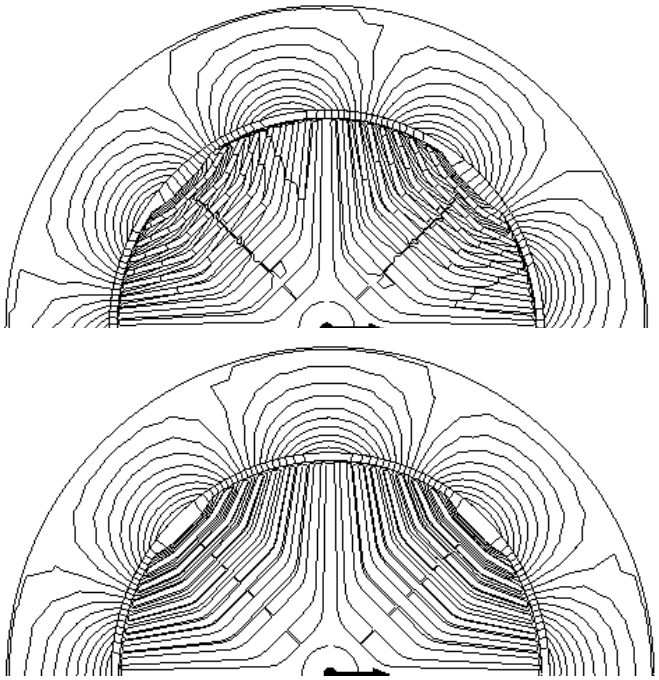

Fig. 11. The 8-pole field flux lines (simplified) at two positions in time, t=0 (top) and t=0+Δt (bottom), corresponding to maximum and minimum torque production points.

The cutout depth in terms of layers is used, and its effect is presented in Fig. 12 and Table III (see Appendix). Finite element solutions and post-processed data (eq. 18) are compared in Fig. 14 and 15, which shows an excellent match, with reduction in torque ripple but also a reduction in mean torque capability.

So by means of design iteration (design *a* through *i* once cutout depth is known) as depicted in Fig. 13, an optimal design, with significantly reduced torque ripple is achieved in design '*i'* and with restored mean torque capability. A simple optimization process by trial and error has been used, in order to modify an existing rotor design which has good performance in a conventionally wound machine. The rib widths and barrier thicknesses have not been altered, the existence of the ribs is simply changed in iteration to find the best result. This is a crude optimization process and improved results may be achieved by using specialist optimization software, however that is beyond the scope of the paper and the very good results presented, have been achieved by hand using information gained from the developed technique.

The mean torque and torque ripple calculations for the various design iterations are tabulated in Table IV (see Appendix). Once the cutout depth is set, the 4-pole flux is somewhat 'choked off' and thus designs *a* through *h* try to re-establish the fundamental flux to regain the mean torque that is lost due to the introduction of the *q*-axis cutout. This is achieved, with the final design *i* having the same mean torque as the original rotor component but with only 44% torque ripple, opposed to the original 106% torque ripple. A comparison of the torque waveforms is presented in Fig. 16.

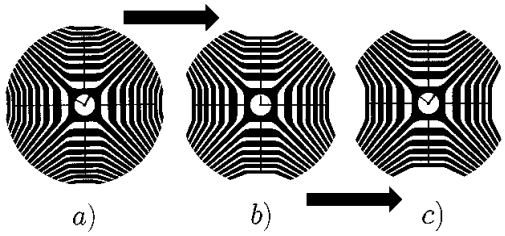

Fig. 12. Cut out depth evolution.

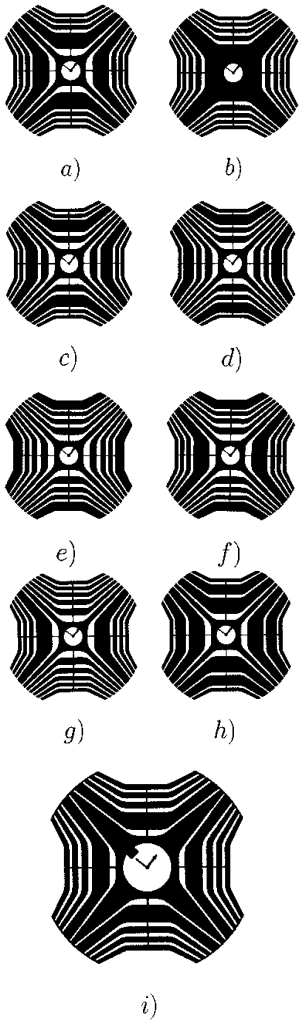

Fig. 13. Rotor designs, with the final design, 'i'. This rotor design has significantly lower torque ripple than the original rotor.

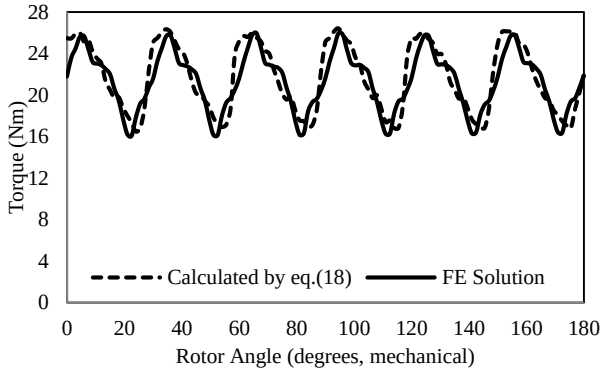

Fig. 14. Cut out depth b) solutions.

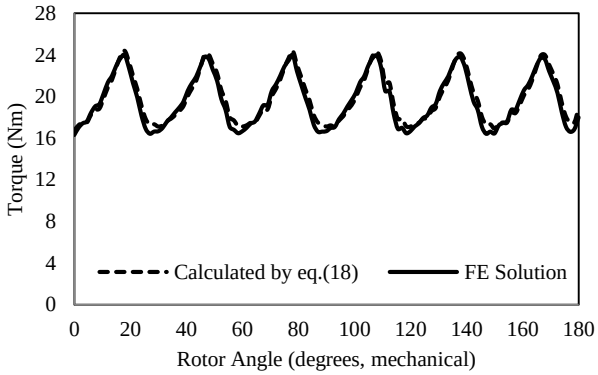

Fig. 15. Cut out depth c) solutions.

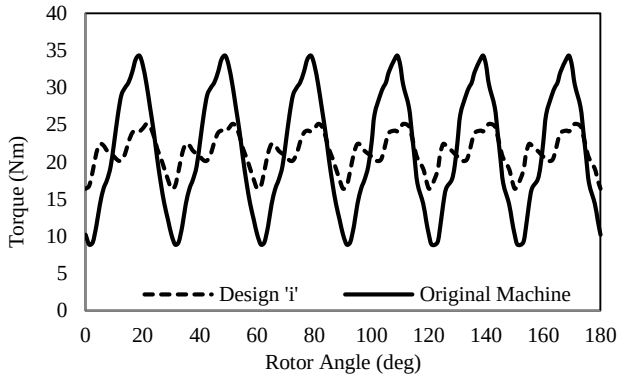

Fig. 16. Comparison of the original design torque waveform and the waveform of design '*i*'.

Through insight given by the developed post-processing technique, which were previously unobtainable, in this example electromagnetic design changes have been made to reduce the interaction of the second order counter-rotating harmonic field, mitigating a large proportion of the torque ripple caused by that harmonic. Therefore, the technique has aided in improving the torque quality of this example topology synchronous reluctance machine.

X. Conclusion

A novel method of analyzing the torque quality of a synchronous machine has been presented. Based on Maxwell stress tensor theory, equations for harmonically related tangential stresses were developed through discrete time Fourier series expressions of the airgap magnetic field. These stress equations where then developed into torque equations that yield valuable information on the torque components and contributions caused by individual field harmonics to the resultant torque waveform.

This post-processing method was then applied to a fractional slot concentrated wound synchronous reluctance machine using automation techniques. A large second order (8-pole) harmonic field was found to be causing the torque ripple, which is information previously unobtainable with conventional methods where only mean torque and torque ripple are the figures of merits available. With the information gained, a direct attack on the second order harmonic can be undertaken and a reduction of torque ripple from 106% to 44% whilst maintaining the mean torque was achieved.

The novel method has been shown to provide valuable information and aid the designer to make more informed decisions on the electromagnetic design changes required to improve machine performance. The developed method can be applied to all synchronous machines and with little modification could be applied to asynchronous machines.

Appendix

A. Finite Element Solution Results for Rotor Designs

Cutout depth increases, reducing torque ripple but also reducing the mean torque capability of the machine.

TABLE III
Cutout Effects (Fig. 12)

Depth (Layers)	Mean Torque (Nm)	Torque Ripple (%)
0	23.10	106.00
1	21.36	46.41
2	19.93	38.93

To re-establish the main d-axis flux to restore torque capability, the existing barriers are 'filled in' to crudely achieve this in trial and error.

TABLE IV
Results (Fig. 13)

Design	Mean Torque (Nm)	Torque Ripple (%)
A	20.24	40.87
B	20.02	45.00
C	20.42	42.22
D	20.63	42.60
E	21.23	43.33
F	20.58	51.71
G	20.10	41.13
H	21.71	45.92
I	22.80	44.00

References

[1] Eason, Hong-Seok Ko; Kwang-Joon Kim, "Characterization of noise and vibration sources in interior permanent-magnet brushless DC motors," *Magnetics, IEEE Transactions on* , vol.40, no.6, pp.3482,3489, Nov. 2004.

[2] Daohan Wang; Xiuhe Wang; Sang-Yong Jung, "Cogging Torque Minimization and Torque Ripple Suppression in Surface-Mounted Permanent Magnet Synchronous Machines Using Different Magnet Widths," *Magnetics, IEEE Transactions on* , vol.49, no.5, pp.2295,2298, May 2013

[3] Chu, W.Q.; Zhu, Z.Q., "Investigation of Torque Ripples in Permanent Magnet Synchronous Machines With Skewing," *Magnetics, IEEE Transactions on* , vol.49, no.3, pp.1211,1220, March 2013

[4] Alotto, P.; Barcaro, M.; Bianchi, N.; Guarnieri, M., "Optimization of Interior PM Motors With Machaon Rotor Flux Barriers," *Magnetics, IEEE Transactions on* , vol.47, no.5, pp.958,961, May 2011

[5] Bianchi, N.; Bolognani, S.; Bon, D.; Pré, M.D., "Rotor Flux-Barrier Design for Torque Ripple Reduction in Synchronous Reluctance and PM-Assisted Synchronous Reluctance Motors," *Industry Applications, IEEE Transactions on* , vol.45, no.3, pp.921,928, May-june 2009

[6] Arkadan, A.A.; ElBsat, M. N.; Mneimneh, M. A., "Particle Swarm Design Optimization of ALA Rotor SynRM for Traction Applications,"

Magnetics, IEEE Transactions on , vol.45, no.3, pp.956,959, March 2009
[7] Lixin Tang; Limin Zhong; Rahman, M.F.; Yuwen Hu, "A novel direct torque controlled interior permanent magnet synchronous machine drive with low ripple in flux and torque and fixed switching frequency," *Power Electronics, IEEE Transactions on* , vol.19, no.2, pp.346,354, March 2004
[8] Jezernik, K.; Korelic, J.; Horvat, R., "PMSM sliding mode FPGA-based control for torque ripple reduction," *Power Electronics, IEEE Transactions on* , vol.28, no.7, pp.3549,3556, July 2013
[9] Hao Zhu; Xi Xiao; Yongdong Li, "Torque Ripple Reduction of the Torque Predictive Control Scheme for Permanent-Magnet Synchronous Motors," *Industrial Electronics, IEEE Transactions on* , vol.59, no.2, pp.871,877, Feb. 2012
[10] EL-Refaie, A.M.; , "Fractional-Slot Concentrated-Windings Synchronous Permanent Magnet Machines: Opportunities and Challenges," Industrial Electronics, IEEE Transactions on , vol.57, no.1, pp.107-121, Jan. 2010
[11] El-Refaie, A.M.; Jahns, T.M.; Novotny, D.W.; , "Analysis of surface permanent magnet machines with fractional-slot concentrated windings," Energy Conversion, IEEE Transactions on , vol.21, no.1, pp. 34- 43, March 2006
[12] Reddy, P.B.; El-Refaie, A.M.; Kum-Kang Huh; Tangudu, J.K.; Jahns, T.M.; , "Comparison of Interior and Surface PM Machines Equipped With Fractional-Slot Concentrated Windings for Hybrid Traction Applications," Energy Conversion, IEEE Transactions on , vol.27, no.3, pp.593-602, Sept. 2012
[13] Shi-Uk Chung; Jong-Moo Kim; Dae-Hyun Koo; Byung-Chul Woo; Do-Kwan Hong; Ji-Young Lee, "Fractional Slot Concentrated Winding Permanent Magnet Synchronous Machine With Consequent Pole Rotor for Low Speed Direct Drive," *Magnetics, IEEE Transactions on* , vol.48, no.11, pp.2965,2968, Nov. 2012
[14] Spargo, C.M.; Mecrow, B.C.; Widmer, J.D., "Application of fractional slot concentrated windings to synchronous reluctance machines," *Electric Machines & Drives Conference (IEMDC), 2013 IEEE International* , vol., no., pp.618,625, 12-15 May 2013
[15] Salminen, P.; Niemela, M.; Pyhonen, J.; Mantere, J., "Performance analysis of fractional slot wound PM-motors for low speed applications," Industry Applications Conference, 2004. 39th IAS Annual Meeting. Conference Record of the 2004 IEEE , vol.2, no., pp. 1032-1037 vol.2, 3-7 Oct. 2004
[16] Magnussen, F.; Sadarangani, C.; , "Winding factors and Joule losses of permanent magnet machines with concentrated windings," Electric Machines and Drives Conference, 2003. IEMDC'03. IEEE International , vol.1, no., pp. 333- 339 vol.1, 1-4 June 2003
[17] Matsuo, T.; Lipo, T.A.; , "Rotor design optimization of synchronous reluctance machine," Energy Conversion, IEEE Transactions on , vol.9, no.2, pp.359-365, Jun 1994
[18] Moghaddam, Reza R.; Magnussen, F.; Sadarangani, C.; , "Novel rotor design optimization of synchronous reluctance machine for high torque density," Power Electronics, Machines and Drives (PEMD 2012), 6th IET International Conference on , vol., no., pp.1-4, 27-29 March 2012
[19] Brown, Geoff; , "Developing synchronous reluctance motors for variable speed operation," Power Electronics, Machines and Drives (PEMD 2012), 6th IET International Conference on , vol., no., pp.1-6, 27-29 March 2012
[20] K. Vogt, "Berechnung elektrischer Maschinen", Wiley VCH, 2007
[21] Griffiths, David J. *Introduction to electrodynamics*. Pearson, 2013.
[22] Meessen, K. J.; Paulides, J. J H; Lomonova, E. A., "Force Calculations in 3-D Cylindrical Structures Using Fourier Analysis and the Maxwell Stress Tensor," *Magnetics, IEEE Transactions on* , vol.49, no.1, pp.536,545, Jan. 2013
[23] Bianchi, N.; Bolognani, S.; Fornasiero, E., "An Overview of Rotor Losses Determination in Three-Phase Fractional-Slot PM Machines," *Industry Applications, IEEE Transactions on* , vol.46, no.6, pp.2338,2345, Nov.-Dec. 2010

Christopher. M. Spargo received the BEng (Hons) degree in Electrical and Electronic Engineering from the University of Newcastle upon Tyne, Newcastle upon Tyne, U.K. in 2011. He is currently pursuing the Ph.D. degree as part of the Power Electronics, Machines and Drives research group at the same university in the School of Electrical and Electronic Engineering. His research interests include the design, modelling and control of switched and synchronous reluctance machines, applied mathematics and electromagnetic theory. He is actively involved with the Institution of Engineering and Technology, UK.

Barrie C. Mecrow received the Ph.D. degree from the University of Newcastle upon Tyne, Newcastle upon Tyne, U.K., for his research into 3-D eddy-current computation applied to turbogenerators. He commenced his career as a Turbogenerator Design Engineer with NEI Parsons, Newcastle upon Tyne, U.K. He became a Lecturer in 1987 and a Professor in 1998 with Newcastle University, Newcastle upon Tyne. He is the Head of the School of Electrical and Electronic Engineering, Newcastle University, where he is also a Professor of electrical power engineering. His research interests include fault-tolerant drives, high-performance permanent-magnet machines, and novel switched reluctance drives. He is actively involved with industry in the aerospace, automotive, and consumer product sectors, who fund a large range of projects.

James D. Widmer is responsible for Newcastle University's 'Centre for Advanced Electrical Drives'. Part of the University's Power Electronics, Drives and Machines Research group, the Centre works with numerous Industry partners to convert academic research into world class products. James' research interests include rare-earth magnet free motor topologies for the automotive industry, including Switched Reluctance and other Motor types, as well as including research into high performance and high efficiency Permanent Magnet machines. James joined Newcastle University in 2009 from a senior post in the Aerospace Industry.